Thermoplastic foaming with thermo-expandable microcapsules: Mathematical modeling and numerical simulation for extrusion process

M. Riou, G. Ausias, Y. Grohens, T. Gaudry, J.-M. Veillé, J. Férec

Version of Record: https://www.sciencedirect.com/science/article/pii/S0009250920303845
Manuscript_c8d755dac352af715f6ec6759efbb1e0

Thermoplastic foaming with thermo-expandable microcapsules: Mathematical modeling and numerical simulation for extrusion process

M. Riou[a,b], G. Ausias[b], Y. Grohens[b], T. Gaudry[a], J.-M. Veillé[a], J. Férec[b]

[a] *Cooper Standard, Route des eaux, 35503 Vitré, France*
[b] *Univ. Bretagne Sud, UMR CNRS 6027, IRDL, F-56100 Lorient, France*

Abstract

A numerical simulation for foaming a melted thermoplastic by extrusion process is conducted, where thermo-expandable microcapsules are used as a blowing agent. Firstly, a growth model for an encapsulated bubble is developed to match experimental results. Then, the growth model is used to numerically solve a 2D non-isothermal die-swell problem, making possible to simulate the extrusion foaming process. In particular, the model is able to predict the foaming location. Numerical results are compared with experimental data obtained by optical microscopy observations and density measurements on extruded samples. The effects of thermoplastic melt rheology on foaming and the die swell induced by foaming are also investigated. This simulation helps to estimate process parameters such as extrusion speed and to predict die swell and sample porosity in whole, to finally optimize the industrial process.

Keywords: Thermo-expandable microcapsules, Growth model, Thermoplastic, Foaming, Extrusion, Numerical simulation, Die swell

1. Introduction

Nowadays, foam materials are competitive materials in industry market and may fulfill some product requirements. Although introduced by Dow Chemical® in the early 1970s [1], Thermo-Expandable Microcapsules (TEM) have recently gained in interest due to their performance and affordability. A TEM is made of a polymeric shell which encapsulates saturated hydrocarbons. Upon heating, the shell softens while internal pressure increases, leading to blow the microcapsule. Compared to other foaming technologies, microstructures created by TEM do not involve cell nucleation and gas diffusion phenomena. It results in a

much more controllable process and product quality. In fact, the cell density is directly managed by the dozing system and the cell size is tailored by TEM composition and process parameters. Furthermore, TEM foaming technology can be performed on every standard extrusion system. However, a more extensive understanding of the foaming behavior during extrusion is necessary to optimize and prevent possible issues during industrial production.

Bubble growth and cavitation problems have been studied for one century. Rayleigh [2] carried out the pioneer work by proposing a simplified bubble radius evolution into an incompressible inviscid liquid. Later, Plesset [3] generalized this relationship by taking into account the surface tension, the liquid viscosity and a non-constant internal versus external pressure difference. Then, Barlow *et al.* [4] combined mass and momentum transfer equations to simulate diffusion phenomena during bubble growth. Street *et al.* [5] modeled a single bubble growth in a non-Newtonian fluid, whereas Patel [6] simplified the single bubble growth in a Newtonian fluid by taking into account Rosner and Epstein assumptions on concentration profile [7]. Amon and Denson [8] introduced a polymer shell in their model to consider the limited amount of available gas when multiple bubbles are growing simultaneously. Arefmanesh and Advani [9, 10] proposed a complete model based on mass, momentum and energy transfer equations. Furthermore, an upper convected Maxwell (UCM) model was used to describe the bubble growth in a viscoelastic fluid. Recently, Kawaguchi *et al.* [11] and then Fujino *et al.* [12] developed models for TEM growth surrounded by air and by a polymer. Up to now, the later work seems to be the most advanced model. They considered mass and transfer equations including diffusion, and used the UCM constitutive equation to represent shell and fluid viscoelasticity.

Only few papers deal with polymer foaming phenomenon during continuous process. The complexity of blowing mechanisms restricts the number of contributions. Ranganathan and Advani [13] modeled a composite, which contains voids in compression molding. Combining Patel growth model [6] and Baldwin fluid model [14], Tsujimura *et al.* [15] proposed a way to estimate the onset position of foam formation in the extrusion die for a PP-isobutane system. Shafi *et al.* [16] and Joshi *et al.* [17] described the nucleation and growth dynamics for batch foaming systems. Shimoda [18] adapted Shafi *et al.* model to the extrusion process. Recently, Uchio *et al.* [19] investigates the TEM foaming phenomenon by extrusion for different PP matrices. For low shear rates and highly viscous polymers they found that expansion can be restricted.

Otherwise, extrudate swell problem for Newtonian fluid is well-known [20, 21, 22, 23]. Die swell is a physical phenomenon due to the velocity profile

rearrangement of a polymer flow subjected to shear stress. Investigations of non-isothermal [24] and compressible flows [25, 26] have been treated. For low Reynolds numbers, Talidorou *et al.* [25] and then Mitsoulis *et al.* [26] showed that strand swelling is not significantly affected by a highly compressible flow, in the sense of pressure dependent. Recently, Tang *et al.* [27] studied and compared 2D and 3D swelling resolution with a PTT model for different width/height die ratio. For high width/height die ratio, they found less deviations between 2D and 3D die swell simulation due to a larger axial velocity than for a low width/height ratio.

In this paper, a microscopic Newtonian thermo-expandable microcapsule growth model is combined with a macroscopic Newtonian flow field simulation. Non-isothermal flow and die swell are considered to estimate the foaming influence on process and material properties. The flow is assumed compressible in the sense of foam dependent. The model is detailed in section 2. The numerical implementation is explained in section 3. Section 4 presents methods and material parameters used in this work. Microcapsule shell viscosity tuning is described in section 4. Die swell, temperature and matrix viscosity influences on foaming flow characteristics are exposed and analyzed in section 5.

2. TEM thermoplastic extrusion foaming model

The aim of this model is to represent the foaming process of TEM embedded inside a thermoplastic matrix during an extrusion process. The global model can be divided into two separate models.

2.1. Microscopic model for a TEM expansion

This model describes the TEM growth at the microscopic scale in a surrounding infinite medium.

2.1.1. Model statements

Fig. 1a shows the top view of a TEM obtained by optical microscopy. A cross section view obtained by scanning electron microscopy is illustrated in Fig. 1b. An outer diameter of 13.4 μm and a shell thickness of 3.0 μm can be measured. The TEM growth is found to contain three phases: an outer polymeric shell, an inner liquid phase and an inner gaseous phase. A schematic representation for an embedded TEM is shown in Fig. 2, where the infinite surrounding fluid is either air or a polymer. For the later case, it is worth mentioning noting that the surrounding medium and the TEM shell are made of two different polymers. The microcapsule growth is driven by the internal pressure, which is related to

the nature of the blowing agent and the microcapsule dimensions. Subjected to elevated temperatures, the internal pressure increases whereas the shell softens. Once the internal pressure is high enough to counteract the external pressure and the shell resistance, the expansion phenomenon occurs. Several assumptions are required to describe the TEM expansion. Most of them are usual assumptions proposed by [11, 12].

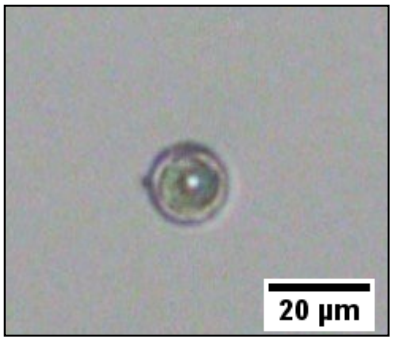

(a) Top view (optical microscopy)

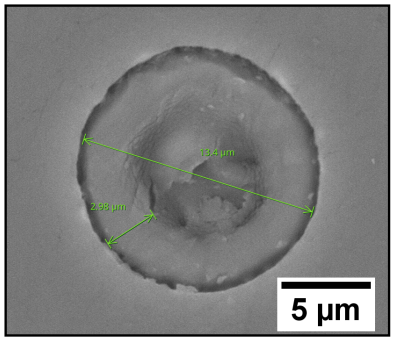

(b) Cross section (scanning electron microscopy)

Figure 1: Microscopic views of a TEM

The model considers one microcapsule with an average behavior, which represents the real expansion for a batch of microparticles inside an infinite fluid.

h1: A TEM is assumed to be a concentric sphere of external radius R_{ext} and internal radius R_{int}, and remains concentric during the expansion. Therefore, a microcapsule grows uniformly along the radial direction r and the velocity vector expressed in a spherical coordinates (r, θ, φ) simplifies to $\vec{V} = V_r(r,t)\vec{e}_r$, where t denotes the time. The interaction between neighboring TEM is neglected.

h2: Gravity and inertial effects are neglected since highly viscous polymers and small particles imply low Reynolds numbers.

h3: Both the shell material (index *sh*) and the surrounding polymer matrix (index *pm*) are supposed to be incompressible Newtonian fluids.

h4: ρ_{sh} represents the shell mass density at room temperature, which is assumed to be temperature independent. The shell material is not damaged during the expansion.

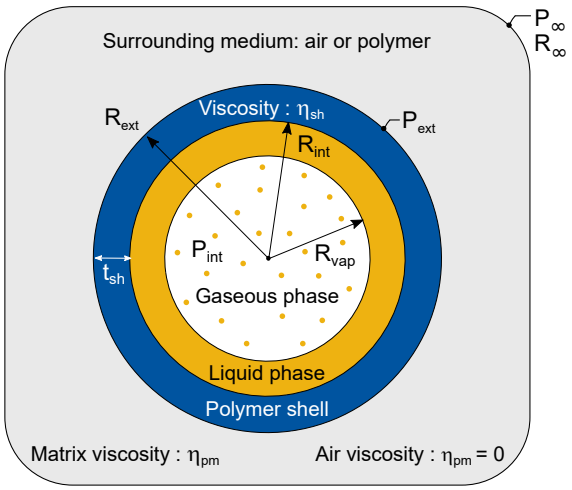

Figure 2: Physical model of a non-isothermal TEM growth

h5: The surface tension γ is neglected. Indeed, shell interfacial tension order-of-magnitude is around $\gamma \sim 10^{-2}$ N/m [28, 12] and therefore $2\gamma/R_{int}$ and $2\gamma/R_{ext}$ terms are around 10^3 Pa, whereas pressure difference is around 10^5 to 10^6 Pa.

h6: The gas diffusion through the shell is not considered.

h7: The blowing agents are miscible in the liquid phase and behave as an ideal gas in the gaseous phase.

h8: The heat flow within the TEM is fast enough to consider the same temperature as the surrounding fluid, and therefore, expansion is assumed isothermal.

Blowing dynamics is ruled by the continuity and the momentum balance equations. Following hypothesis *h*2 and *h*3, these governing equations reduced to

$$\nabla \cdot \vec{V} = 0, \tag{1}$$

$$-\nabla P + \nabla \cdot \underline{\underline{\sigma}} = \vec{0}, \tag{2}$$

where P is the pressure, $\underline{\underline{\sigma}} = 2\eta\underline{\underline{\dot{\varepsilon}}}$ is the deviatoric stress tensor, η the Newtonian viscosity of a material and $\underline{\underline{\dot{\varepsilon}}}$ is the strain rate tensor. In term of spherical coordinates (r, θ, φ), the continuity equation, Eq. (1), yields after simplification

$$\frac{\partial}{\partial r}\left(r^2 V_r(r,t)\right) = 0, \tag{3}$$

which can be rearranged to give after integration

$$V_r(r,t) = \frac{F(t)}{r^2}, \tag{4}$$

where $F(t)$ is a r-independent function. The inner velocity $V_r(R_{int},t) \equiv \dot{R}_{int}$ and the outer velocity at the shell interface $V_r(R_{ext},t) \equiv \dot{R}_{ext}$ can be expressed in function of $F(t)$ such as

$$F(t) = \dot{R}_{int} R_{int}^2 = \dot{R}_{ext} R_{ext}^2. \tag{5}$$

From assumption h1, the deviatoric stress tensor becomes a diagonal tensor with components σ_{rr} and $\sigma_{\theta\theta} = \sigma_{\varphi\varphi}$ (for symmetry condition). Therefore, Eq. (2) can be written as

$$-\frac{\partial P}{\partial r} + \frac{\partial \sigma_{rr}}{\partial r} + \frac{2(\sigma_{rr} - \sigma_{\theta\theta})}{r} = 0\,. \tag{6}$$

2.1.2. TEM expansion in polymer

As suggested by Kawaguchi *et al.* [11] and Fujino *et al.* [12] to tackle the problem of the microcapsule expansion in a polymer matrix, Eq. (6) is integrated between $r = R_{int}$ and $r = R_{ext}$ for the shell domain (index *sh*) and between $r = R_{ext}$ and $r \to \infty$ for the surrounding medium (index *pm*). Thanks to the Chasles theorem, one obtains

$$\begin{aligned} &-P(R_{ext}) + P(R_{int}) + \sigma_{rr,sh}(R_{ext}) \; - \sigma_{rr,sh}(R_{int}) \; + \Delta\sigma_{sh} \\ &-P(R_{\infty}) \; + P(R_{ext}) + \sigma_{rr,\,pm}(R_{\infty}) - \sigma_{rr,pm}(R_{ext}) + \Delta\sigma_{pm} = 0, \end{aligned} \tag{7}$$

where

$$\Delta\sigma_{sh} = 2\int_{R_{int}}^{R_{ext}} \frac{\left(\sigma_{rr,sh} - \sigma_{\theta\theta,sh}\right)}{r} \mathrm{d}r, \tag{8}$$

and

$$\Delta\sigma_{pm} = 2\int_{R_{ext}}^{\infty} \frac{\left(\sigma_{rr,pm} - \sigma_{\theta\theta,pm}\right)}{r} \mathrm{d}r. \tag{9}$$

The stress continuity condition at the inner microcapsule surface requires that $P(R_{int}) - \sigma_{rr,sh}(R_{int}) = P_{int}$ as the surface tension is neglected (h5). At the interface between the outer microcapsule surface and the polymer matrix, a force balance leads to $-P(R_{ext}) + \sigma_{rr,sh}(R_{ext}) = +P(R_{ext}) - \sigma_{rr,pm}(R_{ext})$. The condition of stress continuity at the far-field boundary is $P(R_{\infty}) - \sigma_{rr,pm}(R_{\infty}) = P_{\infty}$, where

P_∞ is the bulk pressure. In the case of extrusion, P_∞ represents the pressure inside the canal. Also, at an infinite distance from the TEM, the stress $\sigma_{rr,\ pm}(R_\infty)$ can be neglected since the polymer deformation is close to zero. Thus, Eq. (7) simplifies to

$$P_{int} - P_\infty + \Delta\sigma_{sh} + \Delta\sigma_{pm} = 0. \tag{10}$$

$\Delta\sigma_{sh}$ and $\Delta\sigma_{pm}$ are obtained from their rheological models. Since a Newtonian behavior is considered for both the shell and the thermoplastic polymer surrounding the TEM (assumption h3), their expressions for the normal stress components are $\sigma_{rr} = -2\sigma_{\theta\theta} = -4\eta F(t)/r^3$. After substituting the relationship for $F(t)$, the integration of Eq. (8) is performed to yield

$$\Delta\sigma_{sh} = -4\eta_{sh}\,\frac{\dot{R}_{int}}{R_{int}}\left(\frac{R_{ext}^3 - R_{int}^3}{R_{ext}^3}\right). \tag{11}$$

On the same way, one obtains the polymer matrix contribution from Eq. (9)

$$\Delta\sigma_{pm} = -4\eta_{pm}\,\frac{\dot{R}_{ext}}{R_{ext}} = -4\eta_{pm}\,\frac{\dot{R}_{int}R_{int}^2}{R_{ext}^3}. \tag{12}$$

When Eqs. (11) and (12) are inserted in Eq. (10), a governing equation for the growth dynamics of a TEM made of a Newtonian shell material inside an infinite Newtonian thermoplastic matrix is

$$\dot{R}_{int} = \frac{R_{int}\left(P_{int} - P_\infty\right)}{4\left[\eta_{sh}\left(\frac{R_{ext}^3 - R_{int}^3}{R_{ext}^3}\right) + \eta_{pm}\left(\frac{R_{int}^3}{R_{ext}^3}\right)\right]}. \tag{13}$$

It is worth mentioning that the upper dot symbol means the total time derivative. When air is considered as the suspending fluid, $\eta_{pm} = 0$ and $P_\infty = P_{atm}$ with P_{atm} the atmospheric pressure, one recovers almost the dynamics growth equation for a bubble surrounded by a shell in air

$$\dot{R}_{int} = \frac{R_{int}\left(P_{int} - P_{atm}\right)}{4\eta_{sh}\left(\frac{R_{ext}^3 - R_{int}^3}{R_{ext}^3}\right)}. \tag{14}$$

This equation is equivalent to Eq. (57a) presented by Elshereff *et al.* [29], and similar to Eq. (12) in terms of the volume of the shell of Amon *et al.* work [8], when the interfacial tension is neglected.

2.1.3. TEM Thermodynamics

According to assumption h7, the blowing agent mixture follows an ideal behavior, therefore each component participates to the global internal pressure. The internal pressure P_{int} is given by the Raoult law such as $P_{int} = \sum P_k$, where P_k is the partial pressure of the k blowing agents. Since the hydrocarbons are mostly in the liquid state at the initial state, the pressure inside a close cavity is determined by the saturated vapor pressure equation. For an ideal mixture, each component contributes to the internal pressure up to their relative partial pressure, which is given for the liquid phase by

$$P_k = P_{sat,k}\, X_{M,k}. \tag{15}$$

In the above equation, $X_{M,k}$ is the molar fraction of for the k^{th} component and $P_{sat,k}$ is its vapor pressure. The saturated vapor pressures for the different components are obtained by the Antoine equation [30]

$$P_{sat,k} = \exp\left(A_k - \frac{B_k}{T + C_k}\right), \tag{16}$$

where A_k, B_k and C_k are Antoine equation constants. The partial pressure can be also expressed in function of the vapor phase by the ideal gas law

$$P_k = \frac{m_{vap,k}\, \mathscr{R}\, T}{M_k\, V_{vap}}, \tag{17}$$

where $\mathscr{R} = 8.314462$ J/(mol $\cdot$ K) [31] is the ideal gas law constant, M_k represents the molar mass of the k^{th} component, V_{vap} and $m_{vap,k}$ denotes the whole volume and the mass of the k^{th} component for the vapor phase, respectively.

When there is presence of liquid phase, a liquid/vapor equilibrium exists, thus Eqs. (15) and (17) are equal. Therefore, $m_{vap,k}$ can be estimated from this equivalence.

$$m_{vap,k} = \frac{P_{sat,k}\, X_{M,k}\, M_k\, V_{vap}}{\mathscr{R}\, T}. \tag{18}$$

As the diffusion phenomenon is neglected (hypothesis h6), the balance for a blowing agent material is given by

$$m_k = m_{liq,k} + m_{vap,k}, \tag{19}$$

where m_k and $m_{liq,k}$ are the total mass and liquid mass of the k^{th} component, respectively. The density of the hydrocarbon mixture is defined by their individual density weighted by their own volume fraction such as

$$\rho_{hc} = \sum_{i=1}^{k} \rho_{liq,k}\, X_{M,k}. \tag{20}$$

In the above equation, $\rho_{liq,k}$ is the density of the k^{th} component. Initially, most of the mixture is in the liquid state, the following approximation can be made

$$m_k|_{t=0} \approx \sum_{i=1}^{k} m_{liq,k}|_{t=0}, \tag{21}$$

where $m_k|_{t=0}$ and $m_{liq,k}|_{t=0}$ are the initial total mass and the initial liquid mass of the k^{th} component at the initial state, respectively. Eqs. (20) and (21) are used to estimate the liquid volume V_{liq} and therefore to approximate the gaseous phase volume V_{vap} with the following conservation relationship $V_{int} = V_{liq} + V_{vap}$, where V_{int} the internal volume of a TEM. By solving iteratively Eq. (19) using Eqs. (20) and (21), $m_{liq,k}$ and $m_{vap,k}$ can be determined at each time.

2.1.4. Blowing dynamics resolution

The total volume of a TEM can be defined as

$$V_{TEM} = V_{int} + V_{sh}, \tag{22}$$

where $V_{TEM} = 4\pi R_{ext}^3/3$, $V_{int} = 4\pi R_{int}^3/3$ and $V_{sh} = 4\pi(R_{ext}^3 - R_{int}^3)/3$ are the external, internal and shell volume of the TEM, respectively. If $R_{ext}|_{t=0}$ and $R_{int}|_{t=0}$ are the initial external and internal radii of a TEM, R_{ext} is (by assuming that the volume of the shell V_{sh} remains constant)

$$R_{ext} = \sqrt[3]{R_{ext}^3|_{t=0} + R_{int}^3 - R_{int}^3|_{t=0}}. \tag{23}$$

The initial contents of hydrocarbons can be evaluated by solving Eq. (19) with the help of Eqs. (18) and (20–22). Once the internal pressure is known, the growth dynamics, Eq. (13), is used to determine the expansion velocity. The internal radius R_{int} is evaluated iteratively to predict the expansion under specific system conditions defined by P_{ext}, T, η_{sh} and η_{pm}. When the liquid is fully evaporated, the internal pressure is only given by the ideal gas law Eq. (17). As the microcapsule continues to grow, the internal pressure begins to decrease until an equilibrium is reached depending on system conditions.

2.2. Macroscopic flow model for a syntactic foam

This section aims to simulate the TEM blowing phenomenon within a thermoplastic for a steady-state flow. A set of hypotheses is addressed to simulate the flow for this syntactic foam (specified by subscript "sf")

H1: The syntactic foam material is considered as an isotropic material.

H2: Gravity and inertial effects are neglected. Indeed, dealing with highly viscous polymer and small particles implies a low Reynolds number.

H3: The density of the suspending matrices is presumed to be temperature independent.

H4: The polymer matrice is assumed to be a slightly compressible Newtonian fluid. The density of the syntactic foam (ρ_{sf}) is dependent on the TEM expansion (R_{ext}). Details are presented in Appendix B.

H5: The viscosity of the fluid is assumed to be not affected by the evolution of ρ_{sf}.

H6: As the Mach number is low for the flow, the work done by pressure is neglected in the energy equation.

H7: Heat capacity (C_p) and thermal conductivity (λ_T) are assumed constant. Neither temperature nor foaming affect both parameters. Regarding the porosity dependency, the extrusion speed is relatively high enough for the outer boundary length and for the low thermal conductivity of polymer melt, to limit the effect of the foaming phenomena on the temperature profile induce by conduction in $y-$direction.

H8: This set of equations gives the quasi-stationary solution.

Following these hypothesis, the governing equations for a non-isothermal flow for a syntactic foam is given by

$$\nabla \cdot \left(\rho_{sf}\ \vec{u}\right) = 0, \tag{24}$$

$$-\nabla P + \nabla \cdot \underline{\underline{\sigma_{sf}}} = \vec{0}, \tag{25}$$

$$\underline{\underline{\sigma_{sf}}} = 2\eta_{app}\underline{\underline{\dot{\varepsilon}}} - \frac{2}{3}\eta_{app}\left(\nabla \cdot \vec{u}\right)\underline{\underline{I}}, \tag{26}$$

$$\rho_{sf}\ C_p\left(\vec{u} \cdot \nabla T\right) - \lambda_T \Delta T = \underline{\underline{\sigma_{sf}}} : \nabla \vec{u}, \tag{27}$$

$$\rho_{sf} = \left[X_{v,TEM}|_{t=0} \cdot \left(\frac{R_{ext}}{R_{ext}|_{t=0}}\right)^3\right] \cdot \left(\rho_{TEM} - \rho_{pm}\right) + \rho_{pm}, \tag{28}$$

where $\vec{u}$ is the fluid velocity vector in a 2D planar geometry with u and v the velocity components in the $x-$ and $y-$directions, respectively. $\underline{\underline{I}}$ is the identity tensor and η_{app} is the apparent shear viscosity determined experimentally through a rheometric slit die. The last term in Eq. (27) describes the heat flux arising from the viscous dissipation. Eq. (28) clearly shows the dependency of syntactic foam density ρ_{sf} on the TEM size evolution R_{ext}.

3. Numerical implementation

3.1. Geometry and boundary conditions

A 2D geometry with a Cartesian coordinate system (x, y) is used to examine the melt flow in a slit die. The channel geometry, shown in Fig. 3, is split in two domains. The left part represents the die, whereas the right one acts for the extrudate at the die exit. Non-isothermal conditions are applied to simulate auto-heating inside the die and cooling at the die exit. The length, the thickness and the width of the slit die are $L_{die} = 60$ mm, $t_{die} = 2$ mm and $W_{die} = 40$ mm, respectively.

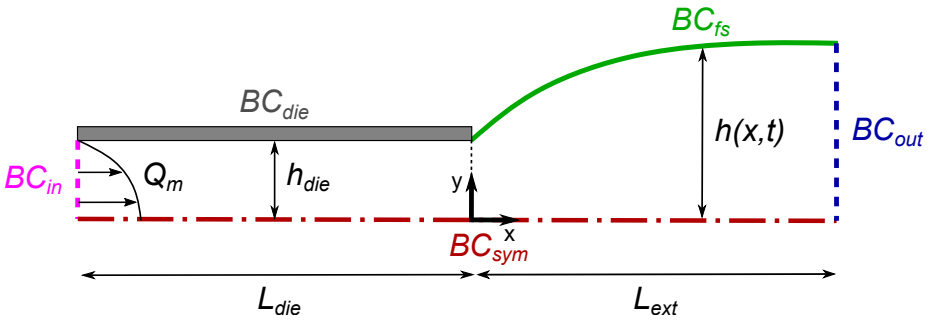

Figure 3: Die swell and foam extrusion model geometry

In the real process, the extrudate enters inside a cold mechanical shaper in a cooled water bath after the die exit. Therefore, the foaming phenomenon is stopped at $L_{ext} = 50$ mm.

3.1.1. Flow boundary conditions

A symmetric boundary condition BC_{sym} is applied along the line at $y = 0$. As the result, the geometry displays only half thickness ($h_{die} = t_{die}/2$). The inlet boundary condition at BC_{in} considers a fully developed flow carrying a fixed mass flow rate $Q_m = < u > W_{die}\, h_{die}\, \rho_{sf}$, where $< u >$ is the average velocity of the melt flow. A no-slip condition, defined by $\vec{u} = \vec{0}$, is applied on the die wall

boundary (BC_{die}). A zero-pressure condition is imposed at the outlet boundary (BC_{out}), which provides for a zero fluid stress along this surface and the back-flow is also suppressed. The BC_{fs} condition consists in a free surface that must satisfy three conditions simultaneously. The conditions of zero shear and normal stresses are prescribed and the zero normal velocity condition is imposed by the following kinetic equation, $\partial h / \partial t + u\, \partial h / \partial x = v$ [32], where $h(x)$ the height of swelling along the $x-$direction. This kinematic condition defines the free surface as a streamline where each element fluid particle remains part of the free surface, and therefore, the particle velocity should always remains tangent to the free surface. One way to handle this issue is to use the arbitrary Lagrangian-Eulerian (ALE) formulation [33, 22, 23]. This method consists in two steps in the sense that the Lagrangian mode allows the mesh to move with the material and then the mesh can freely move as required by the flow domain. The ALE formulation reduces the mesh distortion while tracking material flow. The kinetic equation is implemented in the COMSOL Multiphysics® software using a coefficient form boundary PDE. An artificial diffusion coefficient of $c_{num} = 10^{-5}\mathrm{m/s}^2$ is used to stabilize the computation.

3.1.2. Thermal and thermodynamics boundary conditions

In the extrusion process, a temperature T_{die} is imposed at the BC_{die} surface and along the symmetric axis of the die (BC_{sym}), the surface is insulated from the system. To establish the condition at the flow inlet (BC_{in}), the velocity component along the $x-$direction (i.e., u) for a Newtonian fluid in a steady state regime inside a planar slit die is defined such as

$$u = \frac{3}{2} < u > \left[1 - \left(\frac{y}{h_{die}} \right)^2 \right] , \tag{29}$$

The dissipated heat is given by

$$\underline{\underline{\sigma_{sf}}} : \nabla \vec{u} = 2\eta_{app} \left(\frac{\partial u}{\partial y} \right)^2 = \frac{18\ \eta_{app} < u >^2 y^2}{(h_{die})^4} \tag{30}$$

In case of polymer processing, the heat conduction in the flowing direction (x) is negligible compared to ($\rho_{sf}\ C_p\ u\ \partial T / \partial x$) which corresponds to the convection term [34]. Then, for an equilibrium regime the convection term becomes equal to zero. Thus, after integrating Eq. (27) the fully developed temperature profile at the flow inlet (BC_{in}) is prescribed [34]

$$T_{in} = T_{die} + \frac{3\eta_{app} < u >^2}{2\lambda_T} \left[1 - \left(\frac{y}{h_{die}} \right)^4 \right] . \tag{31}$$

A free convective heat transfer is assumed to the BC_{fs} such as $q = h_{cv} \cdot (T_{amb} - T_{die})$, where T_{amb} the ambient temperature and h_{cv} the convective coefficient for air convection.

Finally, a global constraint condition is applied on the internal pressure inside a TEM to respect the fact that the liquid phase herein is incompressible

$$\begin{aligned} P_{int} &= P_{\infty} \qquad \text{for} \qquad P_{\infty} > \sum_{i=1}^{k} P_k, \\ P_{int} &= \sum_{i=1}^{k} Pk \quad \text{for} \qquad P_{\infty} < \sum_{i=1}^{k} P_k. \end{aligned} \tag{32}$$

As a result, microcapsules are assumed to not collapse under high external pressure.

3.1.3. Solution strategy

The extrusion foaming simulation is illustrated by the flow chart in Fig. 4. A stationary flow solution is first used to determine the velocity and the pressure fields. Then, the macroscopic and microscopic models are simultaneously solved. On the one hand, the ALE formulation computes the free surface whereas the non-isothermal problem Eq. (27) gives the temperature field distribution. On the other hand, the microscopic blowing model predicts the TEM foaming, which modifies the density and therefore the velocity field. It consists in solving Eq. (13) which is implemented in the software through a convection-diffusion PDE type equation and gives the radius R_{int} and the internal volume V_{int} at each position. Eq. (19) is solved using an algebraic differential equation to converge toward a blowing agent state composition and P_{int} is finally determined. An additional step can be appended to stabilize the computation consisting in solving a time-dependent multiphysics model (free surface and non-isothermal flow), before solving simultaneously the macroscopic and microscopic models. The time-dependent solver uses the Backward Differentiation Formula (BDF) algorithm to control the time step and employs a segregated solution approach to solve the system of equations. A non-linear Backward Euler method is applied to approximate the time derivative and each step represents one physics. The first two steps deal with the flow and thermal solutions and then the third step solves the blowing equations Eqs. (13) and (19).

All the computations are carried out on a Dell Precision Tower 7810 workstation, equipped with an Intel® Core™ Intel™ Xeon™ CPU E5-2620 v4 at 2.1 GHz and 128 Go of RAM. The fluid discretization employed for velocity and pressure field is P1 + P1. The default mesh consists of coarse size elements and

Figure 4: Simulation flow chart

is generated and adapted by the software following the physics employed in the simulation (i.e., the mesh close to the no-slip boundary layer, the edges and free surface is made of quadrangle elements, in order to keep an acceptable precision facing strong gradients). In total, the geometry surface is meshed with 10167 elements.

4. Materials and methods

4.1. Thermoplastic matrices

A vulcanized thermoplastic elastomer (TPV) and a polypropylene (PP) matrices have been considered as suspending fluids in this study. Matrices have a different rheological behavior. The thermal conductivity is measured by the hot wire method following EN ISO 22007-1:2017 [35] using Rheograph 20 supplied by Göttfert. The density at room temperature is determined by an AlfaMirage MDS-300 electronic densimeter following ISO standard 1183-1 [36]. PVT measurements are done to determine the melt density (ρ_T) of both thermoplastics in the process temperature range (180-220°C). A capillary rheometer Rheograph 20 is also used to perform rheological, thermal conductivity (λ_T) and PVT measurements. Firstly, a Bagley correction are used to obtain the apparent viscosity η_{app}, then a Rabinowitsch correction considering a power-law shear thinning behavior [37] is applied to determine the true viscosity η_{pm}. In this simulation, because the Newtonian model is considered, η_{app} is applied in the flow computations to obtain the correct pressure profile and η_{pm} represents the bulk viscosity seen by TEM during expansion. Thermal conductivity (λ_T), viscosities (η_{app} and η_{pm}) and melt density (ρ_T) are slightly affected by temperature variations in the range of temperature extrusion (180-220°C). Each characteristic of both polymer matrices is approximated by one average value and Table 1 summarizes the data parameters used for the simulation.

4.2. Thermo-expandable microcapsules (TEM)

A TEM grade has been selected to match temperatures during an extrusion. Expansion behavior has been measured using a hot plate and an optical microscope coupled with a high speed camera. A temperature heating slope of 10 °C/min has been set, ensuring a long time period at elevated temperature, which is roughly equivalent to the residence time of TEM in an extrusion unit. The acquired images are binarized and then analyzed to determine the average TEM behavior in terms of temperature. Fig. 5 depicts the average expansion ratio $\lambda_{ext} = R_{ext}/R_{ext}|_{t=0}$. The expansion curve consists in three differents step. An

Table 1: Properties of the suspending thermoplastic matrices

Material	η_{pm} [Pa · s]	η_{app} [Pa · s]	Q_m [kg/h]	ρ_T [g/cm^3]	C_p [J/(kg · K)]	λ_T [W/(m^2· K)]
TPV	30	90	18.0	0.81	1900	0.190
PP	250	460	11.2	0.76	2400	0.185

abrupt expansion until the liquid phase is evaporated (see Appendix A), then a gently growth due to the pressure increasing along the temperature and a shrinkage due to gas leaking through the TEM shell. To simulate TEM expansion in air, Eq. (13) is used to approximate the bubble growth behavior. Since the viscosity measurements η_{sh} for the pure shell material of the TEM is tricky to perform, η_{sh} is obtained by the inverse method with experimental data. The expression for η_{sh} is reported in Table 2. The form is similar to the Kawaguchi's *et al.* model [11], which considers an Arrhenius dependance of the viscosity with the temperature. The starting temperature and the starting expansion slope are fitted as close as possible to the experimental data and the result (called "Original fit") is shown in Fig. 5. As expected, the model prediction exhibits a higher expansion level attributed to the absence of diffusion (see Fujino *et al.* [12]) and to the choice of a Newtonian behavior for the TEM shell. More accuracy is obtained by adjusting the blowing agent amount, which reduces the liquid reservoir and affects P_{int} when only vapor phase is remaining, as represented by the curve called "Final fit" is shown in Fig. 5.

The effect of viscosity variations on the TEM growth kinetics is shown by Fig. 6. These curves have been computed by considering T = 205 °C as an initial condition. It represents the extreme case where initially $P_\infty > P_{int}$, and then P_∞

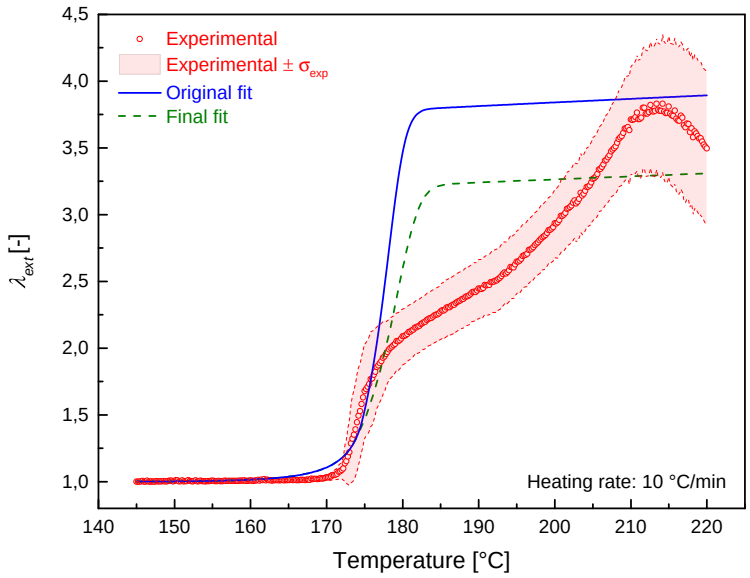

Figure 5: Expansion ratio in term of temperature

decreases infinitively fast until P_{atm}. Fig. 6 clearly indicates the major role of viscosity in expansion kinetics as shown by Kawaguchi *et al.* [38]. When the viscosity is higher the growth is slower and inversely. This shift in time scale can be converted into a shift in temperature behavior. In fact, higher viscosities will apply more resistance to counteract the internal pressure and lead to expansion at higher temperatures.

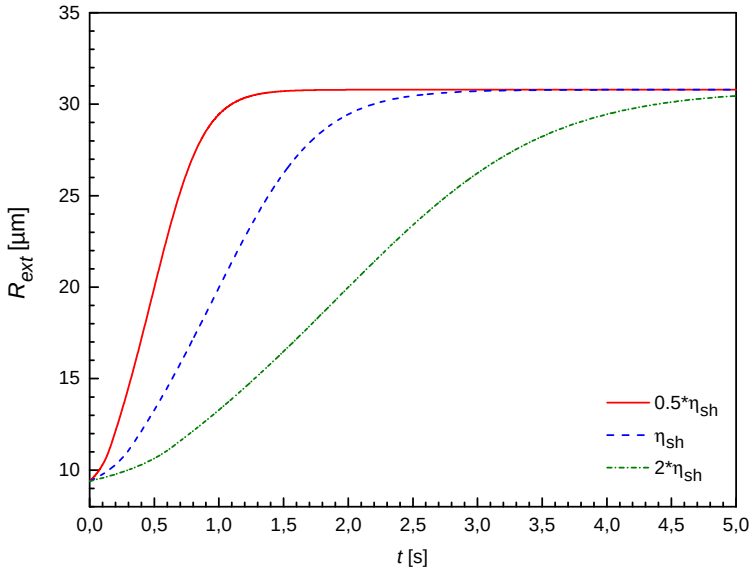

Figure 6: Viscosity influence on TEM growth kinetics.

The initial microcapsule dimensions are measured by laser diffraction and microscopy techniques. $R_{ext}|_{t=0}$ corresponds to the initial average external radius of TEM and $t_{sh}|_{t=0}$ is the initial average thickness of TEM. The density ρ_{sh} is determined after isolating the polymer shell material. It is done by using N,N-Dimethylformamide solvent to remove blowing agents and then, by evaporating it. Since ρ_{sh} and ρ_{liq} are known, the initial density of a TEM computed from volume considerations is estimated at $\rho_{TEM}|_{t=0} = 0.82$ g/cm^3 (see Appendix B).

Gas contents are measured by gas chromatography coupled with a mass spectroscopy. Pentane, isopentane and isooctane are the three gases detected and their properties are reported in Table 3.

For instance the initial state at T = 478,15 K, computed for the blue curve in Fig. 6 is presented in Table 4. m_{liq} and m_{vap} stand for the whole amount in the

Table 2: TEM shell properties

	ρ_{sh} [a] [g/cm^3]	ρ_{liq} [g/cm^3]	$R_{ext}\|_{t=0}$ [a] [μm]	$t_{sh}\|_{t=0}$ [a] [μm]	η_{sh} [$Pa \cdot s$]
TEM	1.20	0.64	9.4	2.4	$\exp(28000/T - 44.3)$

[a] Experimental data

Table 3: TEM blowing agent properties

Substances	k	$X_{M,k}$ [a] [%]	M_k [g/mol]	Antoine parameters [b] A_k [-]	B_k [-]	C_k [-]
Pentane	1	51.5	72.15	20.73	2475.06	-39.94
Isopentane	2	29.7	72.15	20.53	2348.66	-40.05
Isooctane	3	18.8	114.23	20.58	2894.27	-52.41

[a] Experimental data

[b] Antoine parameters are in SI system units (Pa and K) [31]

liquid and vapor phase, respectively. As the blowing agent exists in the liquid phase at the initial state, the internal pressure (P_{int}) can be estimated by using Eqs. (15) and (16) with the parameters given in Table 3.

4.3. Syntactic foam extrusion

The extrusion system is an extruder equipped by a barrier screw (D=60 mm, full length L/D=26) and a dosing system. A slit die with the channel dimensions of $L_{die} = 60$ mm, $W_{die} = 40$ mm and $t_{die} = 2$ mm is used. The cooling bath is located at $L_{ext} = 50$ mm from the die exit and after this distance the syntactic foam microstructure is considered as fixed. The TEM mass fraction is imposed to $X_{m,TEM}$ = 0.65 %. Temperature profile is adjusted to avoid premature expansion inside the extrusion unit. In practice, a temperature at $\pm$ 2 °C is measured manually over 30 s with an infrared pyrometer, at the center of the upper extrudate surface as close as possible to the die exit. Polymer foam melt characteristics are determined experimentally during extrusion process from one pressure transducer located at 10 mm after the slit die entrance. The pressure transducer uncertain-

Table 4: Initial state at 205 °C

Parameters	P_{int} [bar]	m_{liq} [kg]	m_{vap} [kg]	V_{liq} [m^3]	V_{vap} [m^3]
Location $x =$	31.4	$1.71 \cdot 10^{-13}$	$0.74 \cdot 10^{-13}$	$0.27 \cdot 10^{-15}$	$1.17 \cdot 10^{-15}$

ty is $\pm$ 0.5 bar. Density measurements and optical microscopy assessment are done after sample cooling. An optical microscopy image from a cross-section part of an extruded sample for a TPV syntactic foam is illustrated in Fig. 7. A quite good dispersion is observed for the TEM size distribution. The light reflection dots at the center of TEM reveal the presence of remaining shells. The external radius determined by image processing is equal to $R_{ext} = 20.0 \pm 0.4\ \mu$m.

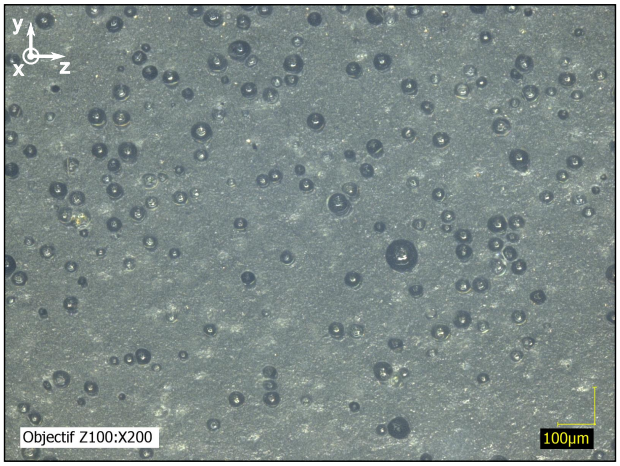

Figure 7: Cross-section part of an extruded sample

5. Results

5.1. Die swell validation for a Newtonian fluid

By computing only step 1 and step 2 (see Fig. 4) or applying $X_{m,TEM} = 0$ %, the extrudate swelling for a Newtonian fluid in both isothermal and non-isothermal conditions by considering the TEM are investigated. A part of the mesh and the final shape of the free surface are presented in Fig. 8. In both cases, the die swell ratio is found to equal 1.186 (see also Fig 16), which is in excellent agreement with the literature value for low Reynolds numbers [20, 22, 26]. The fact that temperature gradient does not affect the die swell is due to the independency of suspending matrix density (ρ_T). Therefore, it implies the same velocity profile in both cases. Note that the swelling occurs in the first 2 mm after the die exit.

5.2. Thermoplastic foaming

Three probes PB_{in}, PB_{end} and PB_{out} are created to evaluate some property values at the flow inlet, the die exit and the outlet problem, respectively. Furthermore, the start points of three streamlines ($SL1$, $SL2$ and $SL3$) are uniformly

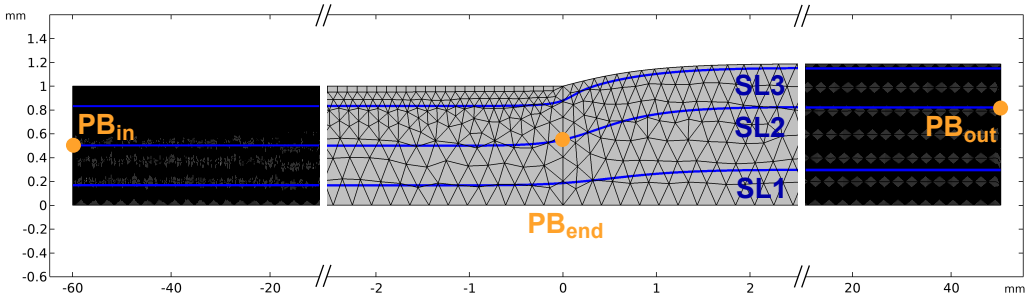

Figure 8: Deformed finite element mesh for the 2D slit die extrusion model

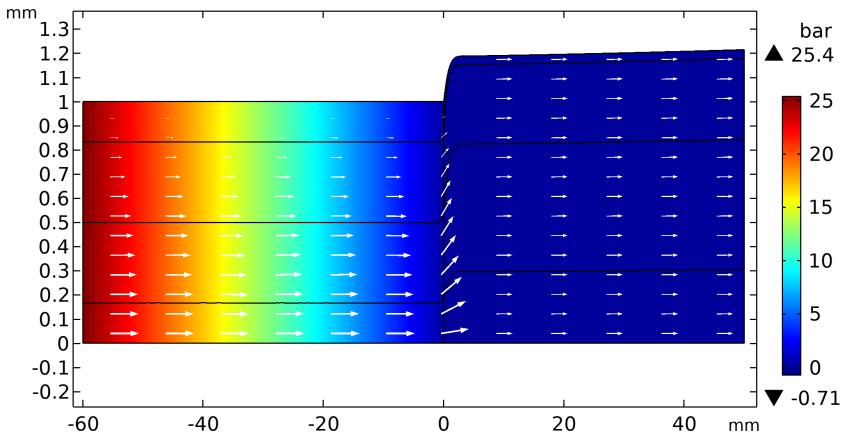

Figure 9: Relative pressure and velocity fields for the field TPV foaming

vertically distributed and are located at $y/h_{die} = 0.25$, 0.50 and 0.75, as depicted in Fig. 8. For all the tested cases, the heat transfer coefficient h_{cv} is set to 150 W/(m^2· K) which corresponds to a forced-air convection, the ambient temperature is set to $T_{amb} = 25$ °C and $T_{die} = 190$ °C.

5.2.1. TPV foaming

The numerical results for the velocity and relative pressure fields and the temperature field are shown in Fig. 9 and Fig. 10, respectively. A linear pressure drop is observed inside the die, which is characteristic for a laminar flow in a slit die. White arrows in Fig. 9 represent the velocity field and are proportional to the velocity magnitude.

The temperature field in Fig. 10 exhibits the viscous effects which increase by 10 to 15 °C the temperature of the thermoplastic melt along the height. The average temperature is found to equal $\overline{T} = 205$ °C at the die exit, and the forced-air convection cools the polymer melt to $\overline{T} = 202$ °C at $x = L_{ext}$.

Around 150 iterations are needed to reach convergence as shown in Fig. 11, where R_{ext} is plotted versus iteration number. Results clearly indicate three different foaming levels for the three probe points. At the die entrance, $R_{ext} = 11.7\ \mu$m, which means the expansion has already started. It could be explained by the fact that pressure at the die entrance is lower than the vapor pressure inside the TEM ($P_{int} \approx 32$ bar). At the die exit, $R_{ext} = 13.8\ \mu$m whereas at $x = L_{ext}$, $R_{ext} = 19.7\ \mu$m. Since the initial TEM radius is 9.4 μm, it means that 45% of the radius growing happens inside the extrusion line and 55% outside.

To explore the TEM growth, the evolution of the external TEM radius along three streamlines (i.e., along the $x-$direction) is plotted in Fig. 12. It is found that the external radius continues to increase if $L_{ext} > 50$ mm. In fact at $x = L_{ext}$, P_{int} is still higher than P_{atm} and therefore the microcapsules continue to grow. Nothing counteracts this expansion because the model does not take into account blowing agent diffusion through the shell, which reduces P_{int}. In practice, the extrudate after $x = L_{ext}$ goes into a cooled mechanical shaper in a water cold bath. Consequently, the temperature decreases sharply and the expansion is stopped. That is why, R_{ext} computed at $x = L_{ext}$ is assumed to be the final TEM radius.

Furthermore, almost no expansion variations are obtained between the three streamlines as shown in Fig. 12. In spite of the temperature gradient along the die height, created by the viscous dissipation, the TEM expansion is not tremendously affected. This is consistent with the low sensibility of the input TEM growth model at elevated temperature (> 190 °C). Additionally, the Newtonian behavior for the shell material leads to an uniform matrix viscosity in the $y-$direction. Following the simulated results, the foamed material would be ho-

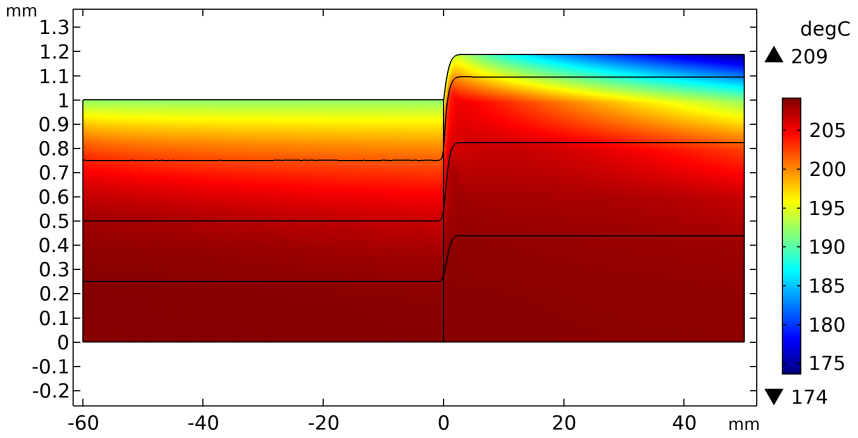

Figure 10: Temperature field for the TPV foaming

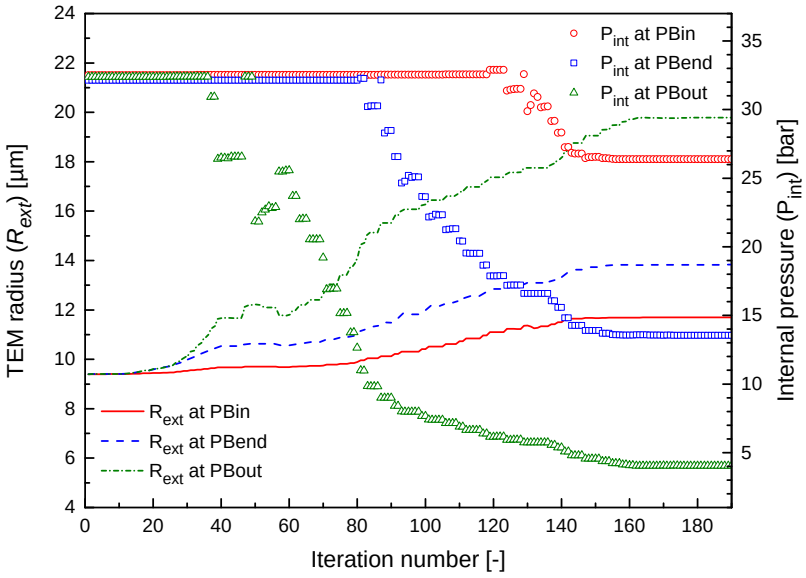

Figure 11: TPV foaming computational resolution

mogeneous. Optical microscopy observations on cross-section of extruded samples show no particle size gradient along the $y-$direction, which is in accordance with the simulation analysis illustrated in Fig. 12. As the growth variation in the $y-$direction is almost insignificant, only results along the streamline SL2 are used in the following discussions. Table 5 summarizes and compares the main flow characteristics with experimental process data. Overall, the predicted flow characteristics are found to be in reasonable agreement with the available experimental data as shown in Table 5. The relative pressure P_∞ and the temperature at the die exit $\overline{T}$ are well described and the porosity is slightly under-estimated. This can be explained experimentally by uncertainties in dosing the amount of TEM and in local porosity measurement. However, these results are acceptable.

Table 5: Comparison between simulation and experimental process data for a TPV foaming

Parameters	P_∞ [bar]	$\overline{T}$ [°C]	$< u >$ [m/min]	Porosity [%]
Location $x =$	-50 mm	0 mm	0	+50 mm
Experiment	22.8	205	9.4	10 ± 0.2
Simulation	21.2	205	9.4	6.1

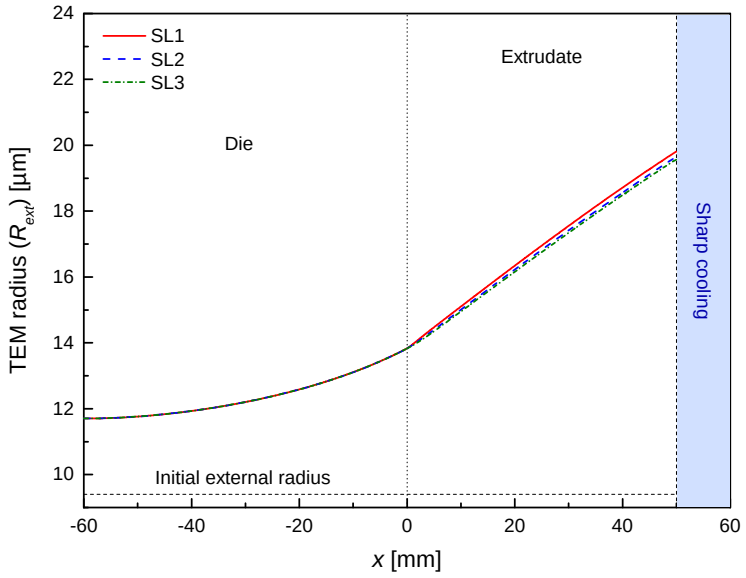

Figure 12: Expansion ratio and porosity along the three streamlines

It is worth mentioning that at $x = L_{ext}$, the average velocity is under-estimated by the simulation ($< u >= 8.0$ m/min). In practice, the extrusion speed is adjusted to counteract the die extrudate swell phenomenon in order to achieve the required part dimensions.

The expansion ratio (λ_{ext}) and the porosity (ϕ) are depicted in Fig. 13. λ_{ext} at $x = L_{ext}$ is clearly limited to 2.1 when compared to 3.5 for air medium surrounding the TEM. In fact, for $< u >= 8$ m/min, it takes 0.375 for the flow to travel the 50 mm out of the die. At the end of the die $R_{ext} = 13.8$ μm. Looking to the growth kinetics (see blue curve in Fig. 6), the time to reach $R_{ext} = 19.7$ μm from 13.8 μm is equal to 0.442 s, which is in accordance with 0.375 s. It means the expansion is limited by the short time spent at high temperature and atmospheric pressure. Then, the porosity evolution is related to the macroscopic volume change due to the TEM expansion. It is found that an increase of 40% of R_{ext} represents only 25% of the final porosity. Under these conditions, it could be concluded that the major part of the expansion occurs after the die exit.

5.2.2. Die swell investigation

The effect of the TEM expansion on the die swell is explored with the numerical model. Fig. 14 depicts the porosity rate in terms of the mass fraction of TEM with values ranging from 0 to 2%. Fig. 15 shows an increase of the average

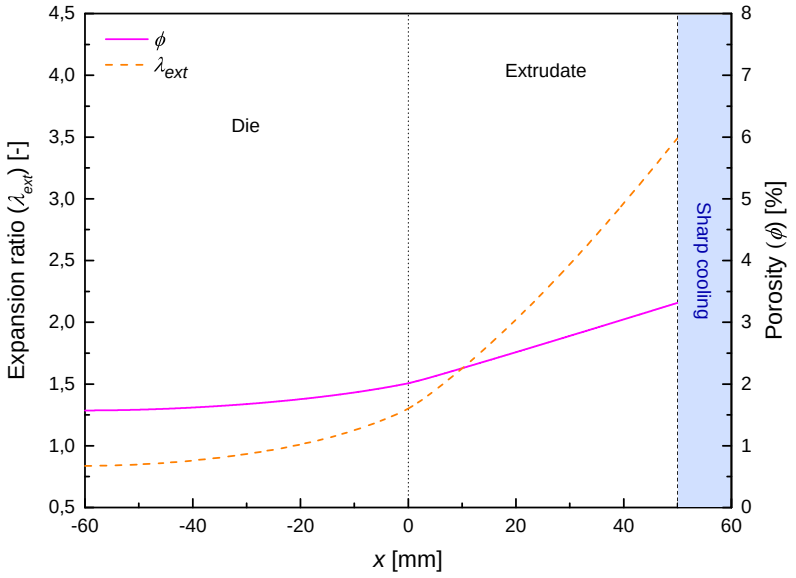

Figure 13: Expansion along the extrusion the SL2 streamline

velocity in function of TEM foaming. This statement could be extended to the flow rate. The die swell increases with increasing the flow velocity as presented in Fig. 16, in which a higher die swell magnitude is observed with a larger TEM content. However, it has to be noticed that the relative increase of the die swell magnitude is lower than the total porosity. In fact, for $X_{m,TEM} = 2.00$ %, $\phi =$ 18.3 % when die swell increasing is 8.5 %.

5.2.3. Temperature influence on thermoplastic foaming

The temperature is found to be a key parameter as it drives the TEM growth. Hence, two others temperatures (T_{die} = 170 °C and T_{die} = 180 °C) are tested to assess the predictability of the numerical model. The final average TEM radius along the height ($\overline{R}_{ext}$) at $x = L_{ext}$ is compared with the mean experimental value measured by image processing in Fig. 17. The average temperature ($\overline{T}$) is determined along the height. The results clearly show a dependence on temperature. As expected, at lower temperature the foaming is lower. In the elevated temperature range of 200-210°C, model predictions and experiments are in good agreement. However, some discrepancies are observed in the lower temperature range of 180-200°C, where the model underestimates the expansion. These differences may come from both the experiments and the numerical model. In fact, there is a lack of information for the true experimental temperature profile

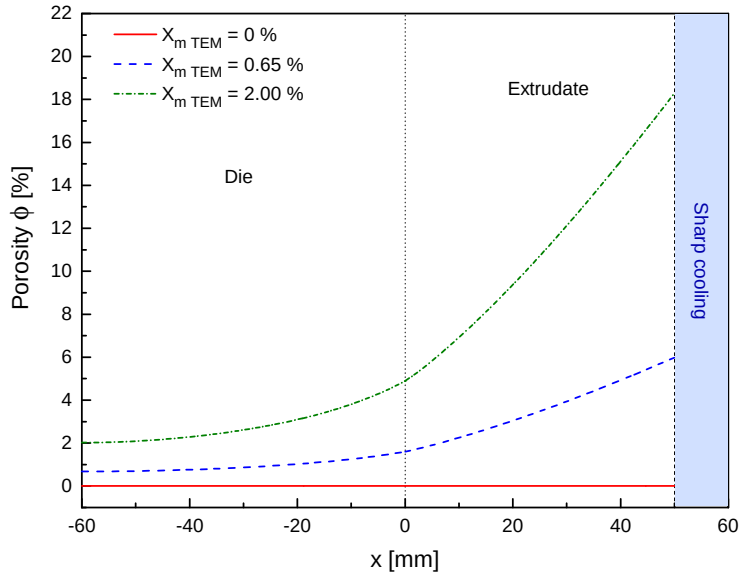

Figure 14: Predicted porosity change along the SL2 streamline

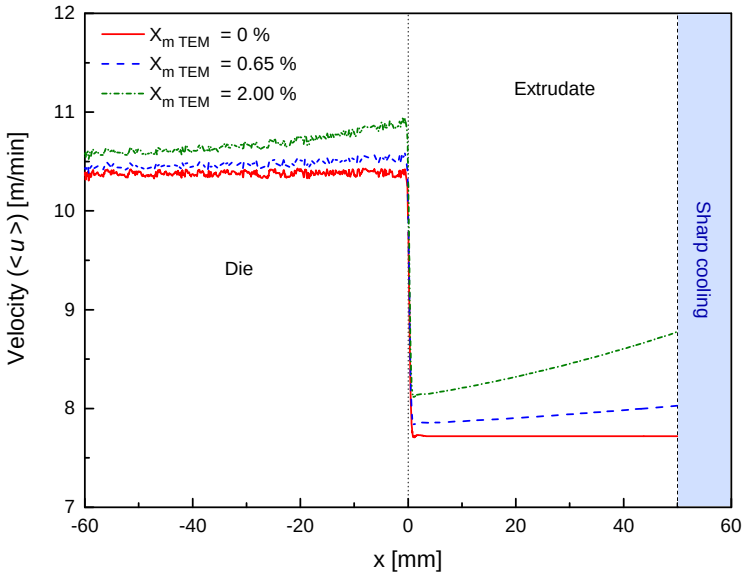

Figure 15: Velocity along a streamline for different amount of TEM (data taken along the symmetry axis)

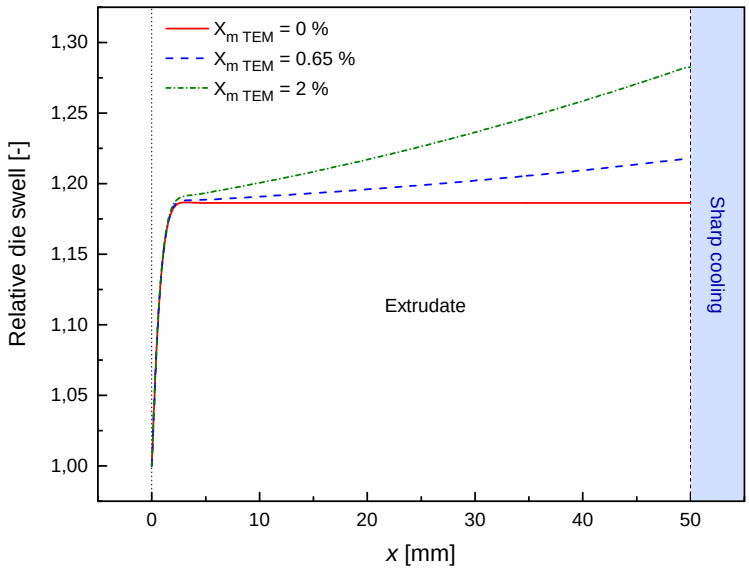

Figure 16: Predicted relative die swell (h/t_{die}) after the die exit

and also an approximation for the TEM growth dynamics (see Fig. 5). Even if the model is not completely accurate quantitatively, qualitative analyses can be conducted.

5.3. PP foaming

For PP foaming simulation, the temperature profile is adapted to fit the same average temperature as for TPV foaming (i.e., 202°C) at $x = L_{ext}$ and therefore, $T_{die} = 174$ °C. Although, this set temperature is lower than the one for the simulation with TPV, the average temperature remains almost the same at the die exit. In fact, since the PP is more viscous, it induces a higher viscous dissipation. This is in accordance with the extrusion experiments and from a practical point of view, a foaming reduction is expected due to this higher viscosity. When compared with TPV results, a higher pressure field is observed for the PP matrix.

Fig. 18 present the temperature along the SL2 streamline for both TPV and PP materials. The temperature is found higher for foaming the PP. This is due to the higher temperature gradient induces by the lower set temperature and the higher auto-heating.

Fig. 19 compare the TEM radius along the SL2 streamline for both TPV and PP materials. Curiously, the external radius of TEM in PP matrix ($\overline{R}_{ext} = 19.9\ \mu$m) is close to the TPV foaming results ($\overline{R}_{ext} = 19.7\ \mu$m). This simulation

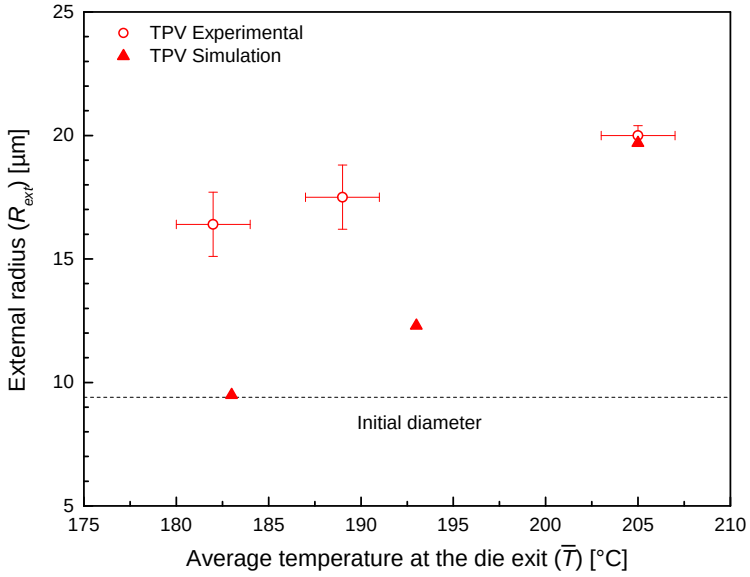

Figure 17: TEM radius in term of average temperature at the die exit

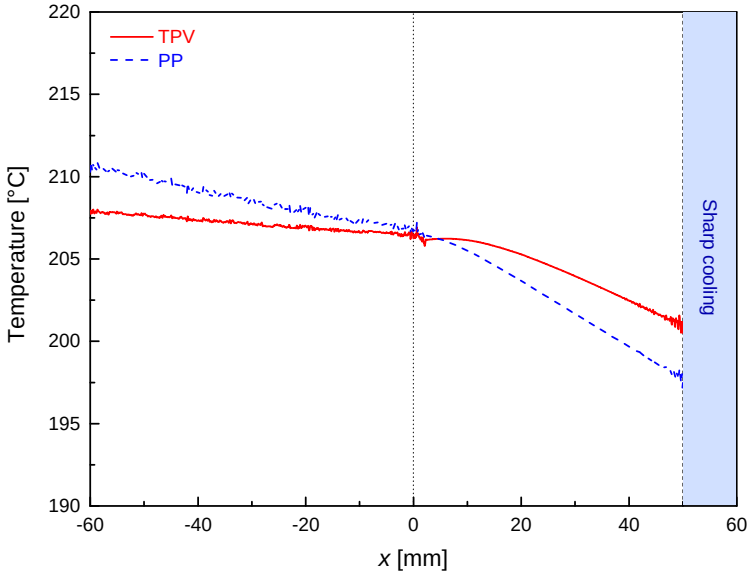

Figure 18: Predicted temperature along the SL2 streamline for the two thermoplastics

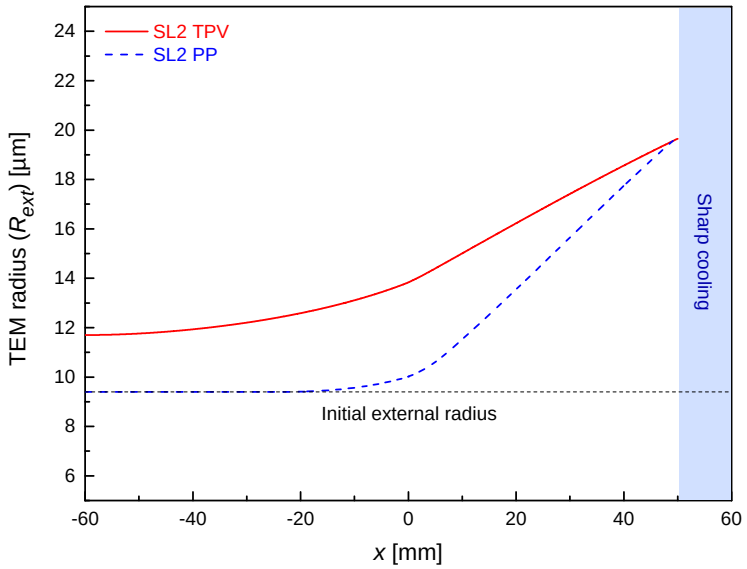

Figure 19: Predicted expansion radius along the SL2 streamline the two thermoplastics

is consistent with the experimental measurements ($R_{ext} = 19.2 \pm 1.1$ μm) on cold samples for this PP matrix. It can be concluded that the viscosity does not affect the expansion level. In practice, for PP foaming around 205 °C, the average external radius of TEM is equivalent to the external radius measured for TPV foaming. This confirms the model predictions, and therefore, the material viscosity appears to be insignificant regarding the final foaming state. These results are summarized in Table 6. Contrary to TPV foaming, the average velocity at the die exit (i.e., $x = 0$ mm) obtained by computations does not fit well with the experimental data. In fact, a strong die swell was experimentally observed for the PP foaming extrusion. The average velocity at $x = L_{ext}$ (i.e., $< u >= 5.3$ m/min) match better with the process data. It means that the Newtonian fluid die swell simulation is more consistent for PP foaming case than for TPV foaming.

Furthermore, Fig. 19 shows a shift of the TEM expansion. In fact, because of the higher pressure due to the higher PP viscosity, the expansion of TEM only starts at the end of the die. It has to be noticed that the expansion for PP matrix occurs mainly after the die exit, consequently the expansion speed is higher. In fact, for $< u >= 5.3$ m/min the time to travel the 50 mm after the die exit is equal to 0,57 s whereas the time to grow from 10 μm to 19.2 μm is equal to 0,80 s following blue curve in Fig. 6. This is due to the higher pressure

difference $P_{int} - P_{\infty}$ induced by the sudden P_{∞} decreasing. Generally speaking, the expansion is faster for a more viscous polymer but catch up the same final level if enough time at high temperature and atmospheric pressure is let to the system.

Table 6: Experimental and predicted process data for a PP foaming

Parameters	P_{∞} [bar]	$\overline{T}$ [°C]	$< u >$ [m/min]	Porosity [%]
Location $x =$	- 50 mm	0 mm	0 mm	+ 50 mm
Experiment	69.6	207	5	10 ± 0.2
Prediction	71.1	204	6.2	6.0

6. Conclusion

In this work, thermoplastic foaming by TEM is investigated by developing a thermo-mechanical blowing model considering Newtonian behaviors. After a viscosity calibration from experimental data of TEM expansion in air, this microscopic growth model is coupled with a non-isothermal macroscopic flow simulation. Representing the real process conditions lead to consistent results compared to experimental measurements. Model predictions indicate that foaming occurs gently inside the die and then it continues after the die for low viscosity thermoplastic whereas for large viscosities the foaming phenomenon is shifted toward the die outside. The die swell phenomenon is promoted by the TEM expansion outside of the die. Overall, the foaming increases the extrusion flow rate when compared with the pure matrix extrusion.

Furthermore, results show that matrix viscosity has no significant influence on foaming for an equivalent temperature profile for the tested conditions. A TPV matrix with a relatively low viscosity produce a syntactic foam with the same porosity than a syntactic based PP matrix with a relatively high viscosity. The explanation comes from TEM shell nature, which is tremendously more viscous than thermoplastic melt and therefore, leads to similar expansion level. From an industrial point of view, material and tooling changes are not key parameters to pay attention in order to ensure a correct foaming. However, TEM are really dependent on temperature and the process temperature should be controlled carefully. It has to be noticed that for higher viscosity of the suspending fluid (i.e., with a more viscous polymer or lower shear rates) and/or lower shell

viscosity, following the model the final foaming state can be affected, as experimentally shown by Uchio *et al.* [19]. Finally, the model suggests that the time at high temperature and atmospheric pressure after the die seems to be an important parameter to enable the TEM to reach their potential higher expansion level.

Despite the strong assumptions made for this model, predictions are in accordance with experimental results. This model can get more accurate by taking into account more realistic material behaviors such as a UCM constitutive equation for modeling the microcapsule growth, a non-Newtonian model to represent the shear-thinning behavior of flowing polymer including viscosity rise outside the die and the gas diffusion through the shell.

7. Acknowledgments

We warmly acknowledge Sekisui Chemical CO., LTD. for their support and their cooperation.

Appendix A. Evolution of internal pressure, liquid and vapor amount

Fig. A.1 shows the evolution of the hydrocarbon phases and the relative internal pressure in function of the temperature during the TEM expansion surrounding by air.

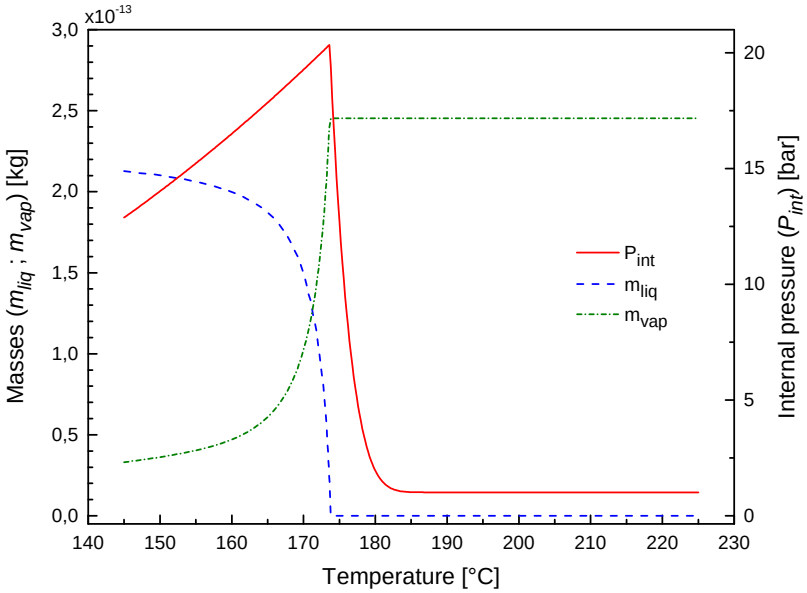

Figure A.1: Evolution of internal pressure, liquid and vapor amount

At the initial state at T = 145 °C the blowing agent is mainly in liquid state. When the liquid phase exists, the internal pressure continues to increase in function of the temperature. Following Fig. 5, the TEM starts to grow at 172 °C, then the liquid is fastly evaporated. As shown in Fig. A.1 the liquid at 175 °C is fully evaporated, then the internal pressure decreases according the growth of the TEM until reaching an equilibrium. This value tends to the external pressure P_∞ which is equal to the atmospheric pressure, as the shell is too thin and too elastic to counteract the expansion.

Appendix B. Calculations of TEM and syntactic foam density

This appendix gives the equations which yield to an expression of the syntactic foam specific mass ρ_{sf} dependent to the TEM expansion and entrance parameters. To begin with, the specific mass ρ_{sf} can be expressed as

$$\rho_{sf} = X_{v,pm} \cdot \rho_{pm} + X_{v,TEM} \cdot \rho_{TEM}, \tag{B.1}$$

where ρ_{pm} and ρ_{TEM} are the specific mass of the thermoplastic and the TEM, respectively. $X_{v,TPV}$ and $X_{v,TEM}$ represent the volume fraction of the thermoplastic and the TEM, respectively. They are related to each others by the following conservation equation $X_{v,pm} + X_{v,TEM} = 1$. Therefore, ρ_{TEM} can be expressed by

$$\rho_{TEM} = \rho_{sh} \cdot X_{v,sh} + \rho_{hc} \cdot X_{v,hc} \tag{B.2}$$

with ρ_{sh}, ρ_{hc} are the mass density of the microcapsule shell and the hydrocarbons, respectively. ρ_{hc} can be expressed as follows

$$\rho_{hc} = \frac{X_{m,hc}}{X_{v,hc}} \cdot \rho_{TEM}, \tag{B.3}$$

where $X_{m,hc}$ and $X_{v,hc}$ are the mass and the volume fraction of the hydrocarbons, respectively. $X_{m,hc}$ and $X_{v,hc}$ are the mass and the volume fraction of hydrocarbons, respectively. Measurements gave $X_{m,hc}$ = 14,1 % and $X_{v,hc} = V_{int}/V_{ext}$. Taking initial values of V_{int} and V_{ext}, gives $X_{v,hc}$ at $t = 0$, denoted by $X_{v,hc}|_{t=0}$, which leads to $\rho_{hc}|_{t=0}$. Combining Eqs. (B.2) and (B.3) allows us to estimate the initial mass density of TEM

$$\rho_{TEM}|_{t=0} = \frac{\rho_{sh}\, X_{v,sh}}{1 - X_{m,hc}} = 820 \text{ kg/m}^3. \tag{B.4}$$

Since the expansion ratio $\lambda_{ext} = R_{ext}/R_{ext}|_{t=0}$, $X_{v,TEM}$ can be also expressed in terms of λ_{ext}

$$X_{v,TEM} = X_{v,TEM}|_{t=0}\, \lambda_{ext}^3. \tag{B.5}$$

Hence, the initial volume fraction of TEM $X_{v,TEM}|_{t=0}$ is equal to

$$X_{v,TEM}|_{t=0} = \frac{V_{TEM}|_{t=0}}{V_{TEM}|_{t=0} + V_{pm}} = \frac{X_{m,TEM}/\rho_{TEM}|_{t=0}}{X_{m,TEM}/\rho_{TEM}|_{t=0} + (1 - X_{m,TEM})/\rho_{pm}}. \tag{B.6}$$

with $V_{TEM}|_{t=0} = 4/3\pi\, R_{ext}|_{t=0}$ the initial TEM volume, V_{pm} the volume of the suspending polymer, $X_{m,TEM}$ the mass fraction of TEM and ρ_{pm} the polymer

mass density. From Eq. (B.5), the evolution of the syntactic foam density is finally given by

$$\rho_{sf} = \left[X_{v,TEM}|_{t=0} \cdot \left(\frac{R_{ext}}{R_{ext}|_{t=0}} \right)^3 \right] \cdot (\rho_{TEM} - \rho_{pm}) + \rho_{pm}, \tag{B.7}$$

References

[1] D. S. Morehouse, R. J. Tetreault, Expansible thermoplastic polymer particles containing volatile fluid foaming agent and method of foaming the same, US Patent 3,615,972 (1971).

[2] L. Rayleigh, VIII. on the pressure developed in a liquid during the collapse of a spherical cavity, The London, Edinburgh, and Dublin Philosophical Magazine and Journal of Science 34 (200) (1917) 94–98. doi:10.1080/14786440808635681.

[3] M. S. Plesset, The dynamics of cavitation bubbles, Journal of applied mechanics 16 (1949) 277–282.

[4] E. J. Barlow, W. E. Langlois, Diffusion of gas from a liquid into an expanding bubble, IBM Journal of Research and Development 6 (3) (1962) 329–337. doi:10.1147/rd.63.0329.

[5] J. R. Street, A. L. Fricke, L. P. Reiss, Dynamics of phase growth in viscous, non-newtonian liquids. initial stages of growth, Industrial & Engineering Chemistry Fundamentals 10 (1) (1971) 54–64. doi:10.1021/i160037a011.

[6] R. D. Patel, Bubble growth in a viscous newtonian liquid, Chemical Engineering Science 35 (11) (1980) 2352–2356. doi:10.1016/0009-2509(80)87016-3.

[7] D. E. Rosner, M. Epstein, Effects of interface kinetics, capillarity and solute diffusion on bubble growth rates in highly supersaturated liquids, Chemical Engineering Science 27 (1) (1972) 69–88. doi:10.1016/0009-2509(72)80142-8.

[8] M. Amon, C. D. Denson, A study of the dynamics of foam growth: Analysis of the growth of closely spaced spherical bubbles, Polymer Engineering and Science 24 (13) (1984) 1026–1034. doi:10.1002/pen.760241306.

[9] A. Arefmanesh, S. G. Advani, Diffusion-induced growth of a gas bubble in a viscoelastic fluid, Rheologica Acta 30 (3) (1991) 274–283.

[10] A. Arefmanesh, S. Advani, Nonisothermal bubble growth in polymeric foams, Polymer Engineering & Science 35 (3) (1995) 252–260.

[11] Y. Kawaguchi, M. Ohshima, M. Tanida, T. Ohishi, A. Ito, T. Sawa, Development of thermally expandable microcapsule and their mathematical models for polymer foaming, Seikei-Kakou 23 (10) (2011) 627–635. doi:10.4325/seikeikakou.23.627.

[12] M. Fujino, T. Taniguchi, Y. Kawaguchi, M. Ohshima, Mathematical models and numerical simulations of a thermally expandable microballoon for plastic foaming, Chemical Engineering Science 104 (2013) 220–227. doi:10.1016/j.ces.2013.09.010.

[13] S. Ranganathan, S. G. Advani, M. A. Lamontia, A non-isothermal process model for consolidation and void reduction during in-situ tow placement of thermoplastic composites, Journal of Composite Materials 29 (8) (1995) 1040–1062. doi:10.1177/002199839502900803.

[14] D. F. Baldwin, Microcellular polymer processing and the design of a continuous sheet processing system, Ph.D. thesis, Massachusetts Institute of Technology (1994).

[15] I. Tsujimura, T. Murayama, T. Zenki, J. Ikeda, M. Ishida, H. Masuoka, A study of bubble nucleation in foam extrusion die., Seikei-Kakou 11 (11) (1999) 937–944. doi:10.4325/seikeikakou.11.937.

[16] M. A. Shafi, K. Joshi, R. W. Flumerfelt, Bubble size distributions in freely expanded polymer foams, Chemical Engineering Science 52 (4) (1997) 635–644. doi:10.1016/s0009-2509(96)00433-2.

[17] K. Joshi, J. G. Lee, M. A. Shafi, R. W. Flumerfelt, Prediction of cellular structure in free expansion of viscoelastic media, Journal of Applied Polymer Science 67 (8) (1998)

1353–1368. doi:10.1002/(sici)1097-4628(19980222)67:8<1353::aid-app2>3.0.co;2-d.

[18] M. Shimoda, I. Tsujimura, M. Tanigaki, M. Ohshima, Polymeric foaming simulation for extrusion processes, Journal of Cellular Plastics 37 (6) (2001) 517–536. doi:10.1106/w4c0-cag6-h3fm-ltjp.

[19] T. Uchio, S. Takiguchi, T. Koda, A. Nishioka, Effect of viscoelastic properties of the base polymer on extrusion foaming with thermally expandable microcapsules, Polymer Engineering & Science (jan 2020). doi:10.1002/pen.25313.

[20] H. J. Park, D. G. Kiriakidis, E. Mitsoulis, K.-J. Lee, Birefringence studies in die flows of an HDPE melt, Journal of Rheology 36 (8) (1992) 1563–1583. doi:10.1122/1.550366.

[21] G. C. Georgiou, The compressible newtonian extrudate swell problem, International Journal for Numerical Methods in Fluids 20 (3) (1995) 255–261. doi:10.1002/fld.1650200305.

[22] V. Ganvir, A. Lele, R. Thaokar, B. Gautham, Prediction of extrudate swell in polymer melt extrusion using an arbitrary lagrangian eulerian (ALE) based finite element method, Journal of Non-Newtonian Fluid Mechanics 156 (1-2) (2009) 21–28. doi:10.1016/j.jnnfm.2008.06.006.

[23] Y. J. Choi, M. A. Hulsen, Simulation of extrudate swell using an extended finite element method, Korea-Australia Rheology Journal 23 (3) (2011) 147–154. doi:10.1007/s13367-011-0018-2.

[24] V. K. Konaganti, M. Derakhshandeh, M. Ebrahimi, E. Mitsoulis, S. G. Hatzikiriakos, Non-isothermal extrudate swell, Physics of Fluids 28 (12) (2016) 123101. doi:10.1063/1.4968826.

[25] E. Taliadorou, G. C. Georgiou, E. Mitsoulis, Numerical simulation of the extrusion of strongly compressible newtonian liquids, Rheologica Acta 47 (1) (2007) 49–62. doi:10.1007/s00397-007-0207-6.

[26] E. Mitsoulis, G. C. Georgiou, Z. Kountouriotis, A study of various factors affecting newtonian extrudate swell, Computers & Fluids 57 (2012) 195–207. doi:10.1016/j.compfluid.2011.12.019.

[27] D. Tang, F. H. Marchesini, L. Cardon, D. R. D'hooge, Three-dimensional flow simulations for polymer extrudate swell out of slit dies from low to high aspect ratios, Physics of Fluids 31 (9) (2019) 093103. doi:10.1063/1.5116850.

[28] D. K. Owens, R. C. Wendt, Estimation of the surface free energy of polymers, Journal of Applied Polymer Science 13 (8) (1969) 1741–1747. doi:10.1002/app.1969.070130815.

[29] R. Elshereef, J. Vlachopoulos, A. Elkamel, Comparison and analysis of bubble growth and foam formation models, Engineering Computations 27 (3) (2010) 387–408. doi:10.1108/02644401011029943.

[30] C. Antoine, Tensions des vapeurs : nouvelle relation entre les tensions et les températures, Gauthier-Villars, Paris, 1888.

[31] NIST, https://physics.nist.gov/, accessed: 2019-12-20 (2019).

[32] R. Keunings, An algorithm for the simulation of transient viscoelastic flows with free surfaces, Journal of Computational Physics 62 (1) (1986) 199–220. doi:10.1016/0021-9991(86)90107-5.

[33] T. J. Hughes, W. K. Liu, T. K. Zimmermann, Lagrangian-eulerian finite element formulation for incompressible viscous flows, Computer Methods in Applied Mechanics and

Engineering 29 (3) (1981) 329–349. doi:10.1016/0045-7825(81)90049-9.
[34] J.-F. Agassant, Polymer Processing 2E: Principles and Modeling, Hanser, 2017.
[35] AFNOR EN ISO 22007-1, Plastics - determination of thermal conductivity and thermal diffusivity - part 1 : general principles (2017).
[36] AFNOR NF EN ISO 1183-1, Plastics - methods for determining the density of non-cellular plastics - part 1 : immersion method, liquid pycnometer method and titration method (2012).
[37] C. W. Macosko, Rheology: Principles, Measurements, and Applications, Wiley-vch, 1994.
[38] Y. Kawaguchi, D. Ito, Y. Kosaka, M. Okudo, T. Nakachi, H. Kake, J. K. Kim, H. Shikuma, M. Ohshima, Thermally expandable microcapsules for polymer foaming-relationship between expandability and viscoelasticity, Polymer Engineering & Science 50 (4) (2009) 835–842. doi:10.1002/pen.21595.